




Single-Differenced Ambiguity Resolution for Orbit Determination of the Haiyang-2B

Hailong Peng, Kecai Jiang , Min Li , Youcun Wang, Xiaomei Wang, Rongxin Fang, Mingsen Lin , *Member, IEEE*, and Qile Zhao

Abstract—In ambiguity resolution, the Hatch–Melbourne–Wübbena code and carrier phase combination is usually used to fix the wide-lane (WL) ambiguity, and thus, the quality of the code observations directly affects the fixing success rate, especially when there are some kind of serious bias errors. Unfortunately, we found that the P1 code multipath (MP) errors of the Haiyang-2B calculated using the MP combination formula rapidly increases from sub-meter to several meters at elevation less than 40°. These rapid variations lead to biases in the fixed WL ambiguities. In this article, we create a static correction map on a grid with 5° x 5° resolution. Using this correction map, we reduced the root mean square of the P1 code bias errors from 1.04 to 0.47 m, which corresponds to an improvement of 54.8%. By comparing the different precise orbit determination solutions, we found that the ambiguity resolution significantly reduced the satellite laser ranging (SLR) residuals from 1.63 to 1.31 cm with an average improvement of 19.6%. However, because of the code errors, the ambiguity fixing rate of the P1 ambiguity-fixed solutions was much lower than that of the C1 solutions. By modeling this static correction, the impact of these errors was effectively reduced. The ambiguity fixing rate for the P1 solutions was improved by 15.6% and a 1–3 mm reduction in the SLR residuals was small but noticeable.

Index Terms—Ambiguity resolution, code bias, Haiyang-2B, onboard global positioning system (GPS), orbit determination.

I. INTRODUCTION

THE Haiyang-2B microwave remote sensing satellite was launched using a CZ-4B rocket on October 25, 2018. In order to obtain high-precision orbit information, the satellite uses an onboard dual-frequency global positioning system (GPS) receiver as its key tracking system. This instrument was independently developed by the Space Star Technology Co., Ltd. and was used on several Chinese satellites, including ZY-3,

Manuscript received February 2, 2021; revised June 25, 2021; accepted July 10, 2021. Date of publication July 14, 2021; date of current version July 28, 2021. This work was supported in part by the Natural Science Foundation of China under Grants 42074032 and 41774035, in part by the Fundamental Research Funds for the Central Universities under Grant 2042021kf0063, and in part by Wuhan Science and Technology Bureau under Grant 2019010701011391. (Corresponding author: Kecai Jiang; Min Li.)

Hailong Peng, Xiaomei Wang, and Mingsen Lin are with the National Satellite Ocean Application Service, Beijing 100081, China, and also with the Key Laboratory of Space Ocean Remote Sensing and Application, Ministry of Natural Resources, Beijing 10081, China (e-mail: phl@mail.nsoas.org.cn; xmwang@mail.nsoas.org.cn; mslin@mail.nsoas.org.cn).

Kecai Jiang, Min Li, Youcun Wang, Rongxin Fang, and Qile Zhao are with the GNSS Research Center, Wuhan University, Wuhan 430079, China (e-mail: kc.jiang@whu.edu.cn; limin@whu.edu.cn; youcunwang1@163.com; rfang@whu.edu.cn; zhaql@whu.edu.cn).

Digital Object Identifier 10.1109/JSTARS.2021.3097082

HY2A, GF-3, GF-7. For low earth orbit (LEO) satellites, the precision orbit determination technique using dual-frequency GPS measurements have been widely used and can provide centimeter-level orbit information. These LEO satellites include the TOPEX/Poseidon [1], [2], CHAMP [3], [4], GRACE [5], [6], SWARM [7], [8], Fengyun-3C [9], and Sentinel-3 [10], [11]. The satellite laser ranging (SLR) residuals, differences between the measured and modeled ranges, can be used for the quality assessment of orbits derived by GNSS techniques, and a 1–3cm consistency of SLR observations and GPS-based precise orbits is demonstrated for a wide range of past and present LEO missions [12].

This reliable, highly accurate orbital information is used in numerous geodetic and remote sensing studies [11]. When there is only one receiver, both the precise point positioning and the orbit determination of the LEO are limited by the ambiguity-float solutions due to inseparable fractional-cycle biases (FCBs) [13]. Fortunately, Ge *et al.* [14] have demonstrated that the FCBs can be separated from the ambiguities using network solutions, and as supplementary products, the acquired FCBs can be used for single-receiver ambiguity fixing. In addition, several similar studies are described by Collins [15] and Laurichesse *et al.* [16]. In general, one method of restoring the ambiguity integer property is to use the FCBs directly, which includes the wide-lane (WL) and the narrow-lane (NL) FCBs. The other method is to use the WL FCBs in combination with the integer-recovery clock products, which already contain the NL FCB information, by fixing the undifferenced ambiguities in advance. Geng *et al.* [17] theoretically proved the equivalence of these two methods. Based on the second method, Montenbruck *et al.* [11] presented an ambiguity-fixed application for the Sentinel-3A satellite and demonstrated a notable improvement in the standard deviation (STD) of the SLR residuals.

The ambiguity resolution has the ability to enhance the observation geometry [18], which improves the quality of the orbit determination. For ambiguity resolution using a single receiver, it is important to eliminate errors first. Previously, this has been done using single-differencing between the navigation satellite pair to eliminate some receiver-end errors, such as the receiver clock errors, and the receiver FCBs, and other common errors also can be weakened. Then, the WL ambiguity is resolved using the Hatch–Melbourne–Wübbena (HMW) combination observable and the multiepoch data [19]–[21]. Thus, the NL ambiguity can subsequently be resolved using the ionospheric-free observable. However, to form the HMW combination observable, the code

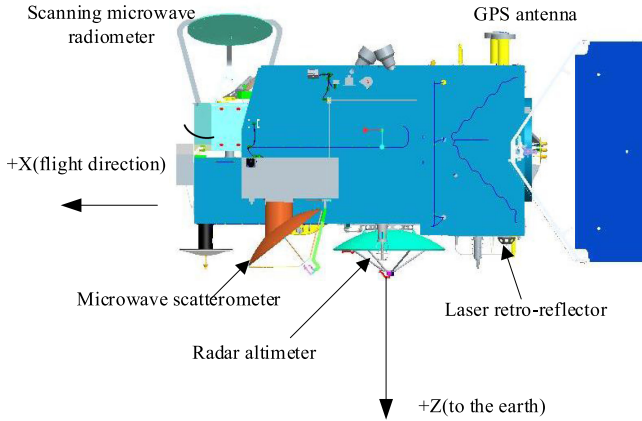


Fig. 1. Haiyang-2B and its payloads.

observations are needed, and thus, the quality of the code observations directly affects the fixing success rate. If the code observations have serious multipath (MP) errors or some kind of bias errors varying with elevation and azimuth and the observation pair used for the single difference has a significantly different elevation and/or azimuth angles, the elimination of these errors is not sufficient, and the residual errors will directly affect the WL ambiguity fixing. Unfortunately, for the Haiyang-2B satellite, we found that the divergences of the $P(Y)$ code and carrier phase in the $L1$ frequency were significantly larger than the C/A code in the $L1$ frequency and the $P(Y)$ code in the $L2$ frequency. We suggest that this might be due to differences in the code tracking loop algorithm.

In this article, we create different ambiguity-fixed precise orbit determination (POD) solutions for the Haiyang-2B satellite using C/A and $P(Y)$ code observations and attempt to weaken the errors in the $P(Y)$ code using a grid correction. Following the introduction of the Haiyang-2B satellite, we analyze the quality of the code data, and investigate the systematic errors using the analysis of the MP effects. Then, we describe the concepts, the mathematical models of the single-receiver ambiguity resolutions, and how the code errors affect it. Finally, we discuss the ambiguity fixing rates and assess the quality of the obtained precise orbits using the SLR data.

II. QUALITY ANALYSIS OF THE CODE OBSERVATIONS

The quality of code observations reflects the performance of the onboard receiver to some extent. In addition, the quality directly affects the POD results because the code observations play an important role in the ambiguity resolution.

A. Platform of the Haiyang-2B Satellite

Haiyang-2B is in a sun-synchronous orbit with an altitude and inclination of about 970 km and 99.34° , respectively. Its main task is the scientific investigation of the ocean environment, including sea winds, waves, currents, sea surface temperatures, tides, and storms. Fig. 1 shows the spacecraft and its payloads, and Fig. 2 shows the receiver and antenna pictures. The onboard GPS receiver, which contains 12 tracking channels for the GPS

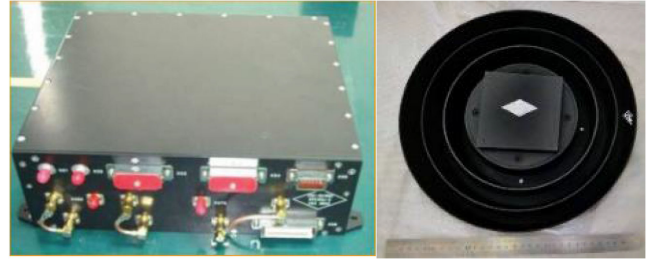


Fig. 2. Onboard receiver and antenna.

TABLE I
PARAMETERS OF THE GPS RECEIVER

Parameters	Values
Frequency	1575.42MHz/1227.6 MHz
Number of channels	12
Sensitivity threshold for acquisition	-162.5dBW
sample frequency	1 Hz
outputting second pulse	$\pm 1\mu\text{s}$
$L1$ phase center (XYZ)	346.74/-179.75/-1375.25 mm
$L2$ phase center (XYZ)	347.34/-177.75/-1396.65 mm
LRA spherical center (XYZ)	311.29/-215.43/986.53 mm
Center of mass (XYZ)	1383.44/6.85/2.35 mm

$L1$ and $L2$ frequencies, offers C/A and $P(Y)$ codes and carrier phase observations in $L1$ frequency, and $P(Y)$ code and carrier phase observations in the $L2$ frequency. Table I gives the parameters of the receiver. In addition, the receiver supports the output of carrier-to-noise observations, but the data are not encoded in the downlink format. For brevity, the C/A and $P(Y)$ codes in the $L1$ frequency are called the $C1$ and $P1$ codes, respectively, and similarly, the $P(Y)$ code in the $L2$ frequency is called the $P2$ code.

In addition, the satellite also carries a laser retroreflector for the SLR. However, unlike the previous Haiyang-2A satellite [22], it does not carry a DORIS instrument. Thus, the GPS instrument is the only way to accomplish POD, which is of great significance for the Haiyang-2B missions, especially for processing altimetry data to invert the sea surface height. A targeted RMS of the final orbit products is 2 to 3 cm in all 3 directions. In addition, in order to pick up the strongest echo signal by the altimeter, the z -axis of the reference frame of the Haiyang-2B points toward the earth's surface, not toward the earth's center. Thus, there is a maximum pitch of 0.167° at northern and southern latitudes of 45° . The x -axis points along the satellite's velocity direction, and the y -axis completes the right-hand system.

B. Measurement Noise

Because the accuracy of the carrier phase observations is much higher than that of the code observations, the method we adopt to assess the measurement noise is as follows. First, we subtract the carrier phase observations from the code observations at 1 s intervals. Then, we difference between the adjacent epochs to obtain the noise sequences. Finally, we set the time window as two minutes and slide the window to compute the STDs.

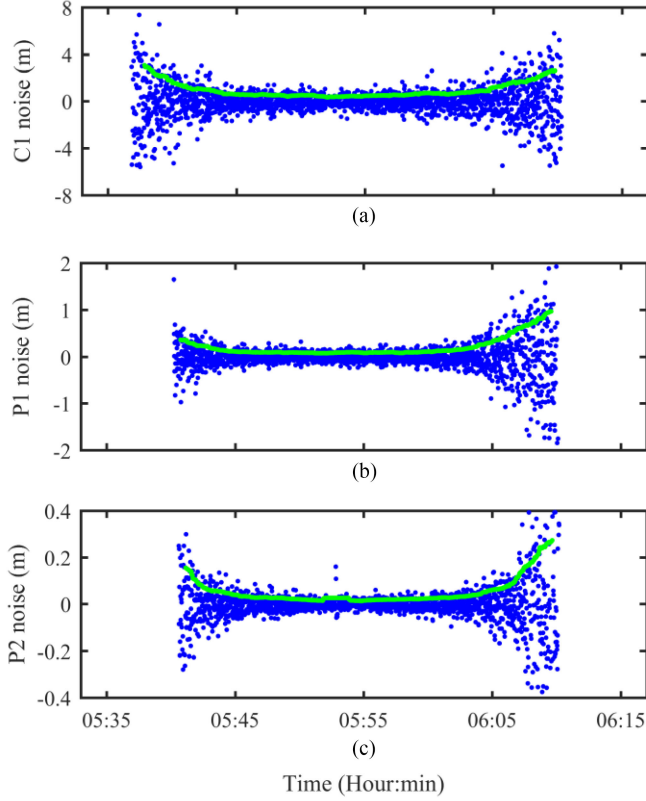


Fig. 3. G05 measurement noise (blue dots) for the $C1$, $P1$, and $P2$ code observations for the pass on November 10, 2018. The green line indicates the STD of the two-minute sliding window.

Taking the satellite whose pseudorandom noise code is G05 in GPS constellation as an example, Fig. 3 shows the measurement noise and STDs of the three types of code observations for a pass on November 10, 2018. This plot illustrates the increased code noise level at lower elevations as the satellite rises and sets. As can be seen from Fig. 3, the $C1$ code contains the most noise, followed by the $P1$ code, and the $P2$ code contains the least noise. There is a difference of roughly 4 to 5 times in noise level between the different codes.

To further clarify this difference, we also created histograms of the STDs of the two-minute sliding window and the corresponding probability cumulative curves in Fig. 4. The histogram peaks are 0.456–0.504 m for $C1$, 0.087–0.101 m for $P1$, and 0.021–0.025 m for $P2$. The STD minimum values are 0.314 m for $C1$, 0.065 m for $P1$, and 0.013 m for $P2$. Ninety percent of the STDs are less than 1.91 m for $C1$, 0.55 m for $P1$, and 0.13 m for $P2$. The noise level of $P1$ is 4 to 5 times smaller than that of $C1$, and 4 to 5 times larger than that of $P2$. Thus, if we only consider the noise level, compared to the $C1$ code, the $P1$ code observations are more suitable for the ambiguity fixing process for the Haiyang-2B satellite.

C. Code Analysis Based on MP Combination and Modeling

In addition to the measurement noise, the MP is one of the most common errors in the code observations. The MP combination can be used to eliminate the effects of ionospheric

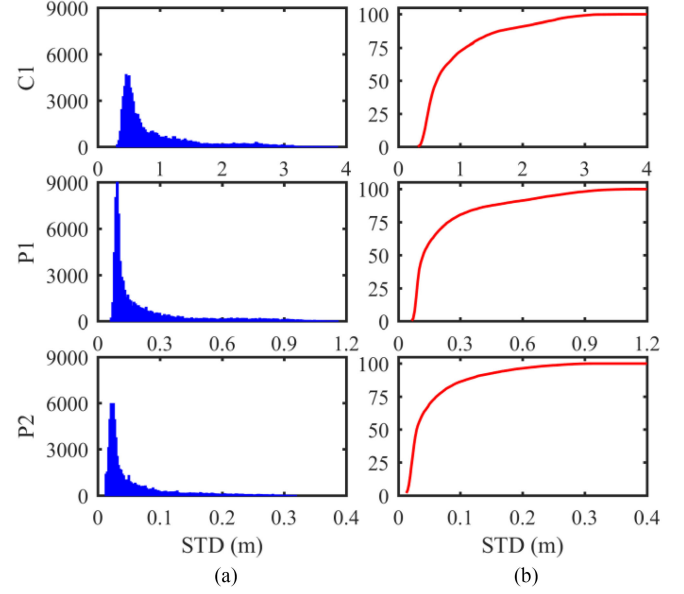


Fig. 4. $C1$, $P1$, and $P2$ code measurement noise statistics for satellite G05 of three days, from November 10, 2018 to November 12, 2018. (a) Histograms of the STDs of the two-minute sliding window, unit: epoch numbers. (b) The corresponding probability cumulative curves, unit: %.

delay and geometric distance based on single-frequency code observations and dual-frequency carrier phase observations [23]. In addition, it can reflect the matching degree between the code and the carrier phase observations intuitively. The combination can be expressed as

$$\begin{aligned}
 MP_i &= p_i - \frac{f_i^2 + f_j^2}{f_i^2 - f_j^2} \phi_i + \frac{2f_j^2}{f_i^2 - f_j^2} \phi_j - D_{ij} D_{ij} \\
 &= -\frac{f_i^2 + f_j^2}{f_i^2 - f_j^2} \lambda_i (N_i + B_{r,i} - B_{,i}^s) \\
 &\quad + \frac{2f_j^2}{f_i^2 - f_j^2} \lambda_j (N_j + B_{r,j} - B_{,j}^s)
 \end{aligned} \tag{1}$$

where p and ϕ are the code and the carrier phase observations in meters, respectively; λ and f are the wave-length and the frequency in meters per cycle and Hz, respectively; N is the integer ambiguity in cycles; B_r and B^s are the receiver- and GPS satellite-end carrier phase fractional cycle biases in cycles, respectively; and the subscripts i and j denote the different frequencies. It should be noted that the computed MP errors include the residual noise of the code observations, and that if there are some biases between the code observations and the carrier phase observations, these errors are also included in the computed MP errors.

Using (1), we can compute the MP errors of the three types of code for the Haiyang-2B satellite. Fig. 5 demonstrates that the G05 MP errors of the three types of code vary with elevation angles. As can be seen from the figure, there is some deviation in the $P1$ code. When the elevation angle is less than 40° , the $P1$ code MP errors rapidly increase from the submeter level to a few meters as the elevations decrease. This leads to the inconsistency between the $P1$ code observations and the other

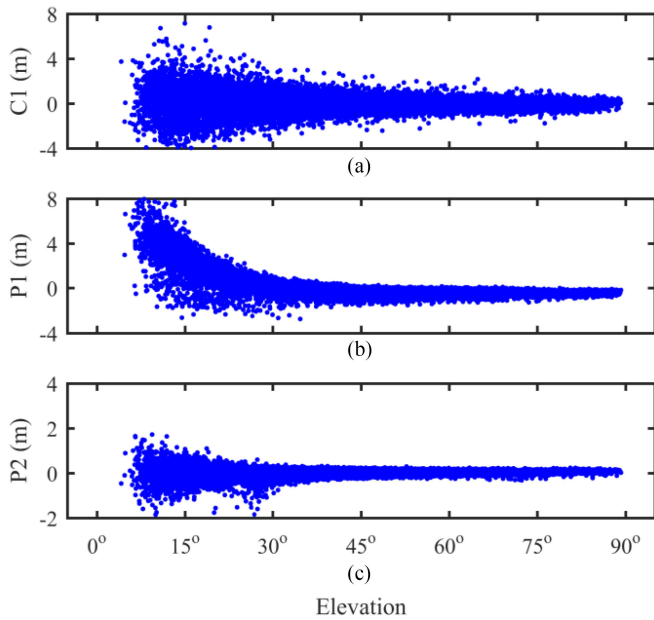


Fig. 5. G05 MP errors versus elevation angles using the data for November 2018.

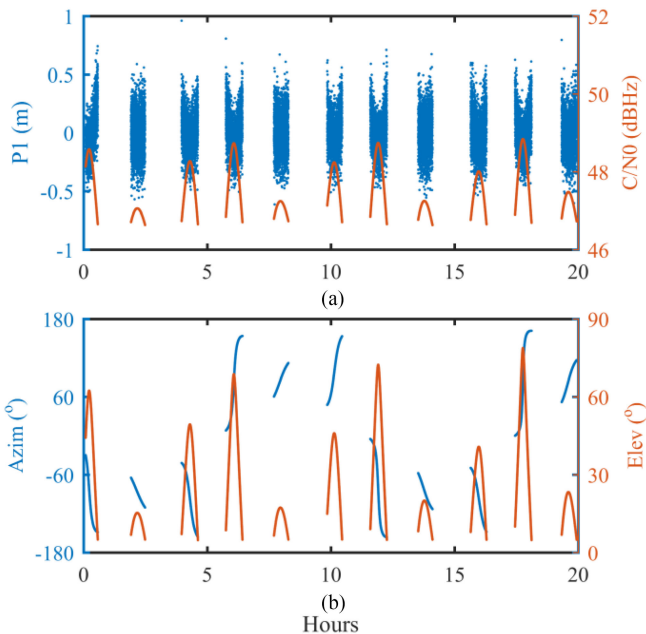


Fig. 6. Errors in Spirent simulation without the delay of ionosphere and troposphere using the same type of GPS receiver.

two code observations at low elevation angles. The constant bias of this inconsistency could be eliminated by a single-difference operation during the ambiguity fixing processing, but this approach did not work for the rapid variation part.

For further verification, we used the same type of the onboard GPS receiver to connect to the Spirent simulation source for testing without the delay of ionosphere and troposphere, and Fig. 6 shows the errors in the $P1$ code observations. As seen from the figure, there is also some deviation at low elevation angles in $P1$ simulation data. The deviation is significantly

smaller than that of the in-orbit data, possibly because the signal strength is relatively stable in the simulation environment. We suggest that the rapid variations in $P1$ code observations may be related to the code tracking loop algorithm. Since the GPS adds a W code modulation to the original P -code, that is the $P(Y)$ code, the receiver accomplishes the $P(Y)$ code and the $L2$ carrier phase tracking through semi-codeless technology [24]. For the GPS receiver on the Haiyang-2B, the $P2$ code tracking uses the third-order delay-locked loop method, which consists of a phase discriminator, a loop filter, and a numerically controlled oscillator. The $P1$ code tracking did not use a loop filter, but simply processed the result of the phase discriminator and directly controlled the phase delay of the local pseudo-code signal to accomplish the P -code closed-loop adjustment. Thus, the accuracy of the $P1$ code observations is lower than that of the $P2$ code observations. In addition, this tracking design reduces the sensitivity of the code tracking and leads to loss of lock at low elevations when the signals became weaker. However, the carrier phase assisted pseudocode tracking method used for the P -code slows down the process of loss of lock of the $P1$ code, which decreases the code's accuracy and gradually increases the system's deviation, as seen in Fig. 5. Because the signal acquisition threshold is higher than the tracking threshold, the phenomenon occurring when the navigation satellite enters the field of view is slightly better than that when it leaves the field of view. It should be noted that these errors are difficult to separate from MP errors.

However, we found that there was a stable pattern that depends on the line-of-sight directions of the satellite in normal orbit, and the static errors can be modeled using a grid map in an antenna-fixed reference frame. The details of the estimation method can be found in [25]. In order to verify the stability of the pattern of the Haiyang-2B satellite, first, we estimated the map on a grid with a $5^\circ \times 5^\circ$ resolution for every month from November 2018 to March 2019. We found that the differences between the maps varied from a few centimeters to a decimeter, and thus, the stability was sufficient for correction modeling. Since this is not the focus of our study, the differences between the maps are not shown here.

Fig. 7 shows the average map of the $P1$ code based on the five months of early data. As can be seen from the figure, there is an obviously elliptical area in the center of the map, and the two ends of the area point to azimuths of 90° and 270° . In this area, the errors mainly varied by 10 to 20 cm. There is also a valley along the axis of the area, in which the errors reach a minimum, about -0.3 m; while the errors reach a maximum of close to 3 m in the crescent area. In addition, for the rest of the map, the errors vary from 0.5 to 1 m. In order to further verify the stability of the error in $P1$ code, the data of April and May 2021 are used in Fig. 8. By comparing the two figures, it can be seen that although the time span of the two sets of data is more than two years, the variation of the error of $P1$ code is very similar.

In addition, we estimated the map on a grid with a $5^\circ \times 5^\circ$ resolution, so there were 1297 grid points, corresponding to 1297 parameters to be estimated. Fig. 9 shows the distribution of the amount of observed data related to the individual grid parameters

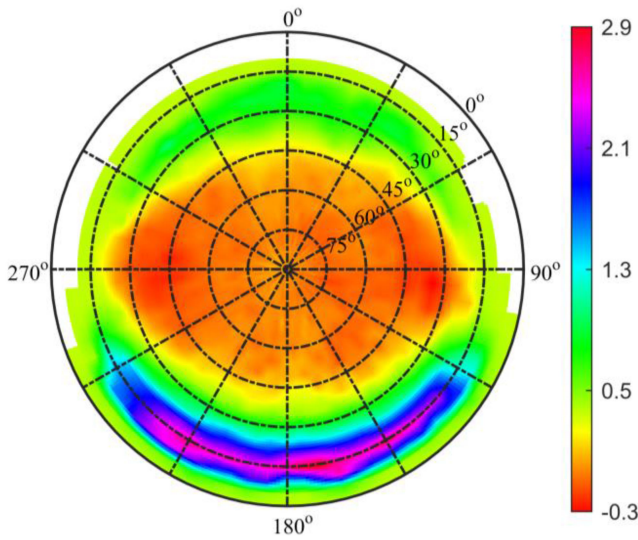


Fig. 7. Average map of the $P1$ code (unit: m) based on five months of early data. The azimuth angle of 0° indicates the velocity direction of satellite Haiyang-2B, and the blank areas indicate insufficient data.

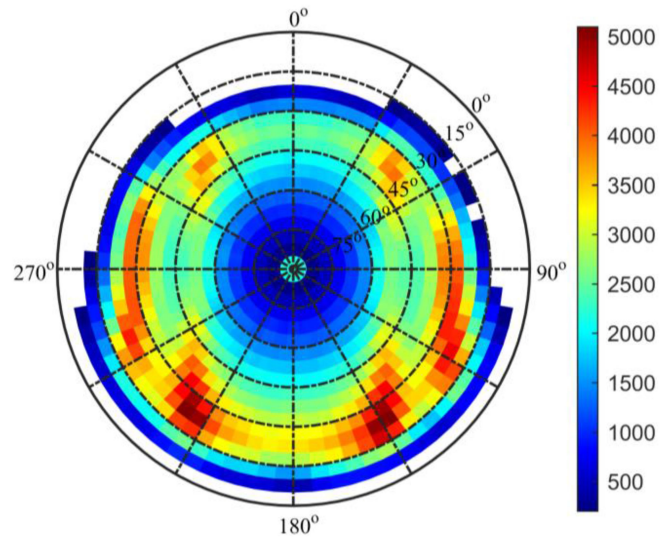


Fig. 9. Distribution of the number of observed data related to the individual grid parameters of the model based on one month's data. The blank area is less than 200.

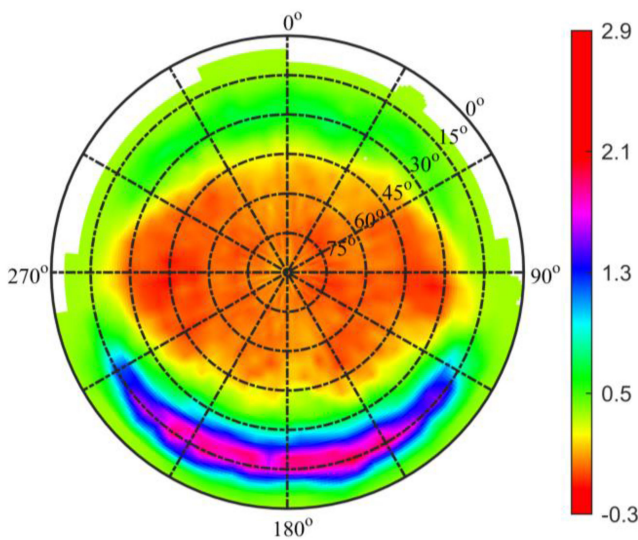


Fig. 8. Average map of the $P1$ code (unit: m) based on data from April and May 2021. The azimuth angle of 0° indicates the velocity direction of satellite Haiyang-2B, and the blank areas indicate insufficient data.

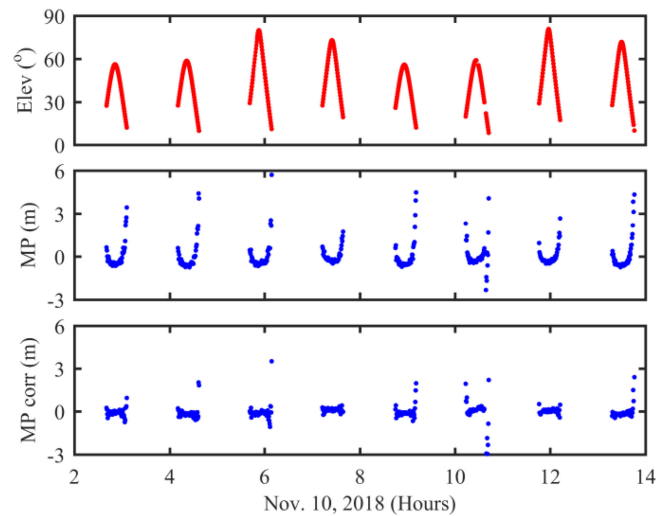


Fig. 10. Elevation angles and the errors of the $P1$ code without and with the $5^\circ \times 5^\circ$ grid corrections varying with time on November 10, 2018.

based on one month's data. In the figure, the data volume in the edge and central areas is the lowest, but also above 200, while that in mid-elevations can reach 3000 to 4000. Therefore, even if only one month's data is used to estimate the parameters, there is still a high data redundancy.

Fig. 10 shows a comparison of the errors with and without the map corrections for G05. As can be seen from the figure, the correction effect is significant, and the deviations at low elevations are significantly suppressed. By correcting for the bias errors, we decreased the mean RMS value of the November data from 1.04 to 0.47 m showing an improvement of 54.8%. The corrected values greater than 2 m account for less than 2% of the errors.

For comparison, Fig. 11 shows the average map of the $C1$ and $P2$ codes based on five months of early data. The values are mostly ± 10 cm. The $C1$ code is not symmetric in azimuth and increases from an azimuth of 0° to 180° . The $P2$ code shows three peak fringes. This may be due to the design of the GPS antenna. However, since the error is relatively small, unlike the $P1$ code, it is difficult for it to cause a bias in the WL ambiguities of the ambiguity resolution. However, we also obtained the grid map of the $C1$ and $P2$ codes based on the data of April and May 2021. Again, that was not different from Fig. 11, so we did not presented the figure here.

In addition, in order to verify whether these errors were related to the signal dynamics, we also analyzed the line-of-sight acceleration variations between GPS and HY2B. As can be seen in Fig. 12, taking G21 as an example, the range of the line-of-sight

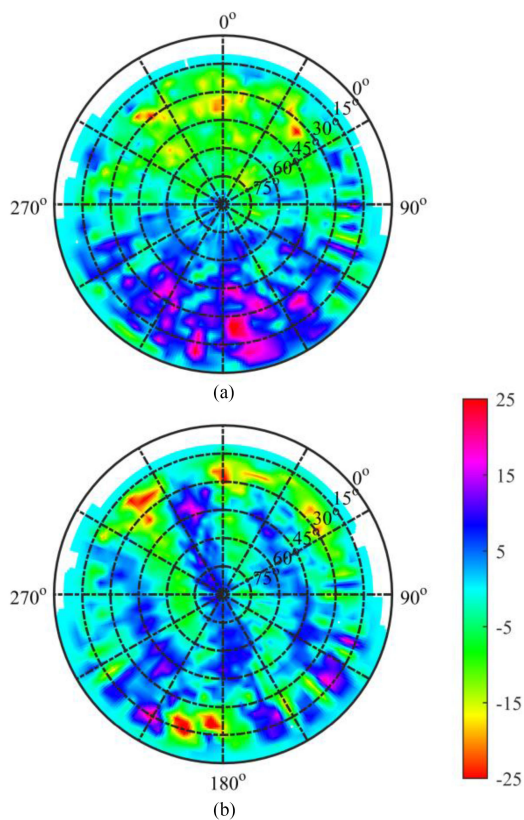


Fig. 11. Average map of the (a) C1 and (b) P2 codes (unit: cm) based on five months of early data, the azimuth angle of 0° respects the velocity direction of the Haiyang-2B.

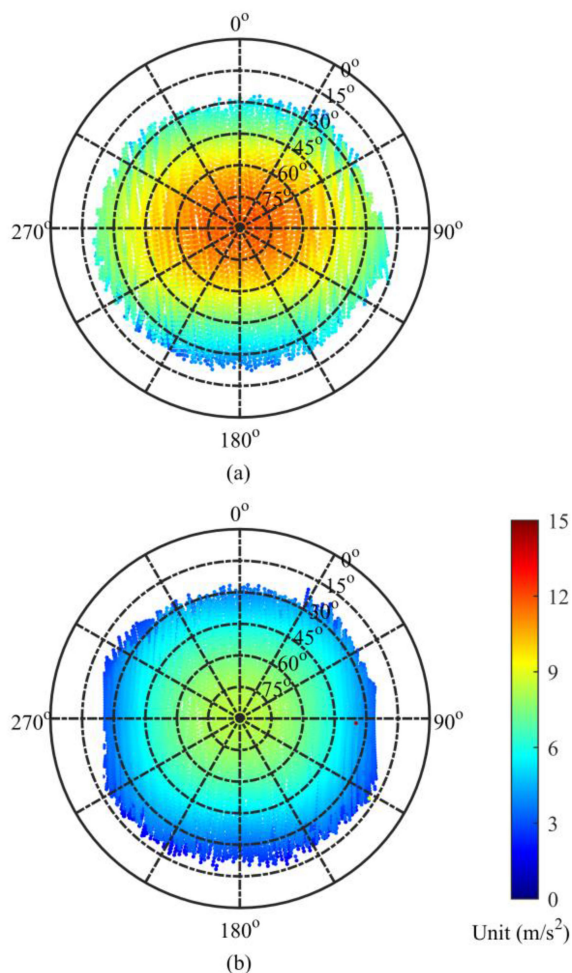


Fig. 13. Sky-view map of the line-of-sight acceleration of G21. (a) Based on data from November 2018. (b) Based on data from March 2019.

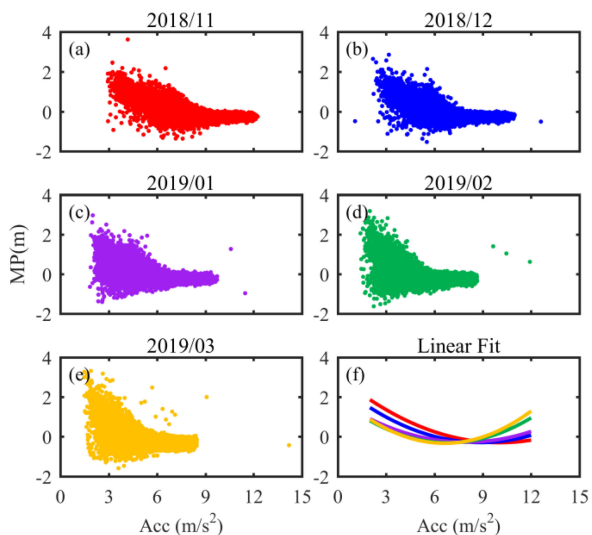


Fig. 12. G21 MP errors versus the line-of-sight acceleration for five months of data.

acceleration is not fixed, which decreases from a maximum of 12 to 8 m/s² for five months of data. Considering just two subplots for November and December 2018, an error proportional to the line-of-sight acceleration may be suspected. However, as the range of the acceleration goes down, this correlation with

acceleration is not apparent in the remaining subplots, and the difference of the linear fitting curves also increases gradually.

For further comparison, Fig. 13 shows the acceleration maps for November 2018 and March 2019. Although it not obvious, there is an elliptical region in the middle of the November map, similar to Fig. 7. That makes the errors appear to have a certain correlation with the acceleration. However, for the March map, it has become azimuth independent, which is not consistent with the static pattern of the errors. That also explains why the errors are not correlated with the acceleration. Therefore, it turns out that these errors cannot be described as a function of a single variable such as the line-of-sight acceleration.

III. AMBIGUITY FIXING METHODOLOGY

As mentioned above, we found that the P1 code observations of the Haiyang-2B suffered serious bias errors. These directly affect the HMW combination function and reduce the success rate of ambiguity fixing. Here, we introduce the observation equations with the biases involved in the single-receiver ambiguity resolution.

A. Observation Models

Normally, the undifferenced observation equations of the code and the carrier phase between the receiver and the navigation satellite at epoch t for frequency j are

$$\begin{aligned} p_{r,j}^s(t) &= \rho_r^s(t) + T_r^s(t) + c[dt_r(t) - \delta\tau^s(t)] \\ &\quad + \frac{A}{f_j^2} + b(e, z) + \zeta_{r,j}^s(t) \\ \phi_{r,j}^s(t) &= \rho_r^s(t) + T_r^s(t) + c[dt_r(t) - \delta\tau^s(t)] \\ &\quad - \frac{A}{f_j^2} + \lambda_j N_{r,j}^s + \lambda_j B_{r,j} - \lambda_j B_{j,j}^s + \varepsilon_{r,j}^s(t) \end{aligned} \quad (2)$$

where the subscripts r and s are used to distinguish between the receiver and the GPS satellite, respectively; c is the velocity of light in meters per second; and ρ is the geometric distance between the receiver and the GPS satellite in meters. T and A are the tropospheric delay and the ionospheric delay, respectively; dt and $\delta\tau$ are the receiver and satellite clocks in seconds; $b(e, z)$ denotes the static code bias errors for an elevation angle e and an azimuth z ; ζ and ε are the residual noises of the code and carrier phase observations, respectively; and the other symbols are the same as (1).

In LEO applications, the ionospheric-free combination is usually used to eliminate the first-order ionospheric delay and it is the basic observation equation for the precision orbit determination. The tropospheric delay and the high-order ionospheric delay are often neglected. In addition, the HMW combination is often used for cycle slip detection and WL ambiguity fixing. The two combination observables can be expressed as

$$\begin{aligned} p_{\text{IF}} &= \frac{f_1^2}{f_1^2 - f_2^2} p_1 - \frac{f_2^2}{f_1^2 - f_2^2} p_2 \\ \phi_{\text{IF}} &= \frac{f_1^2}{f_1^2 - f_2^2} \phi_1 - \frac{f_2^2}{f_1^2 - f_2^2} \phi_2 \\ \phi_{\text{HMW}} &= \frac{f_1}{f_1 - f_2} \phi_1 - \frac{f_2}{f_1 - f_2} \phi_2 - \frac{f_1}{f_1 + f_2} p_1 - \frac{f_2}{f_1 + f_2} p_2 \\ &= \lambda_{\text{HMW}}(N_{\text{HMW}} + B_{r,\text{HMW}} - B_{\text{HMW}}^s) - b_{\text{HMW}} \\ N_{\text{HMW}} &= N_1 - N_2, B_{r,\text{HMW}} = B_{r,1} \\ &\quad - B_{r,2}, B_{\text{HMW}}^s = B_{,1}^s - B_{,2}^s \\ \lambda_{\text{HMW}} &= \frac{c}{f_1 - f_2}, b_{\text{HMW}} = \frac{f_1}{f_1 + f_2} b_1 + \frac{f_2}{f_1 + f_2} b_2 \end{aligned} \quad (3)$$

where p_{IF} and ϕ_{IF} are the ionospheric-free observables of the code and the carrier phase observations in meters, respectively; ϕ_{HMW} is the HMW observable in meters; the indices 1 and 2 are the $L1$ and $L2$ frequencies, respectively; and λ_{HMW} is the WL wavelength, approximately 86.2 cm for the GPS $L1$ and $L2$ combination. In addition, the relationship between the float ionospheric-free ambiguity, the $L1$ frequency ambiguity, and the HMW ambiguity can be expressed as

$$\lambda_{\text{IF}}(N_{\text{IF}} + B_{r,\text{IF}} - B_{\text{IF}}^s) = \frac{f_1^2}{f_1^2 - f_2^2} \lambda_1(N_1 + B_{r,1} - B_1^s)$$

$$\begin{aligned} &- \frac{f_2^2}{f_1^2 - f_2^2} \lambda_2(N_2 + B_{r,2} - B_2^s) \\ &= \frac{c}{f_1 + f_2} (N_1 + B_{r,1} - B_1^s) \\ &\quad + \frac{f_2}{f_1 + f_2} \lambda_{\text{HMW}}(N_{\text{HMW}} + B_{r,\text{HMW}} - B_{\text{HMW}}^s). \end{aligned} \quad (5)$$

The weight of ϕ is usually much greater than that of p in the POD processing. Here, we determined the weight according to the observed noise level of code and carrier phase observations. Since the carrier phase model contains the ambiguity, careful consideration should be given to quality control, such as cycle slips. The details of quality control models and stochastic models can be found in [26], and we did not repeat them in the article.

B. Ambiguity Resolution

According to the above equations, the major problem in ambiguity fixing is that the FCBs of the carrier phase observations are absorbed by the ambiguity estimates of the single receiver. Fortunately, the receiver FCBs can be eliminated using the single-differenced observations, and the single-differenced FCBs of a certain satellite pair can be obtained based on the network solutions [14]. Then, the recovery of the integer properties of the ambiguity can be determined. The single-differenced equations of (4) and (5) are

$$\begin{aligned} \Delta\phi_{\text{HMW}} &= \lambda_{\text{HMW}}(\Delta N_{\text{HMW}} - \Delta B_{\text{HMW}}^s) - \Delta b_{\text{HMW}} \\ \Delta N_{\text{HMW}} &= \frac{1}{\lambda_{\text{HMW}}}(\Delta\phi_{\text{HMW}} + \Delta b_{\text{HMW}}) + \Delta B_{\text{HMW}}^s \end{aligned} \quad (6)$$

$$\begin{aligned} \lambda_{\text{IF}}(\Delta N_{\text{IF}} - \Delta B_{\text{IF}}^s) &= \frac{f_1}{f_1 + f_2} \lambda_1(\Delta N_1 - \Delta B_1^s) \\ &\quad + \frac{f_2}{f_1 + f_2} \lambda_{\text{HMW}}(\Delta N_{\text{HMW}} - \Delta B_{\text{HMW}}^s) \Delta N_{\text{IF}} - \Delta B_{\text{IF}}^s \\ &= \frac{f_1}{f_1 + f_2} (\Delta N_1 - \Delta B_1^s) \\ &\quad + \frac{f_1 f_2}{f_1^2 - f_2^2} (\Delta N_{\text{HMW}} - \Delta B_{\text{HMW}}^s), \text{ with } \lambda_{\text{IF}} = \lambda_1 \end{aligned} \quad (7)$$

or

$$\begin{aligned} \Delta N_1 - \Delta B_1^s &= \frac{f_1 + f_2}{f_1} (\Delta N_{\text{IF}} - \Delta B_{\text{IF}}^s) \\ &\quad - \frac{f_2}{f_1 - f_2} (\Delta N_{\text{HMW}} - \Delta B_{\text{HMW}}^s) \end{aligned} \quad (8)$$

where Δ denotes the single-differenced operator; and ΔN_1 and ΔN_{HMW} are the NL and WL ambiguities, respectively.

In the article, we used the daily WL satellite bias (wsb) and the high-rate clock (30 s) products provided by the Centre National d'Études Spatiales/Collecte Localisation Satellites (CNES/CLS) to eliminate the FCB errors. Thus, the first step is to fix the float WL ambiguity to an integer using (6) with the multi-epoch data for each pass after correcting the single-differenced WL FCBs by the CNES wsb products. The next step is to substitute the fixed WL integer ambiguity into (8) and

combine the float ionospheric-free ambiguity derived using the CNES clock products to obtain the fixed NL integer ambiguity. It should be noted in this step that due to the CNES clock products including the narrow-lane FCB correction information, the float ionospheric-free ambiguity is no longer affected by the NL FCB errors and ΔB_1^s in (8) can be ignored. When the WL and NL ambiguities have both been fixed to an integer, the related ionospheric-free integer ambiguity can be recovered using (7). Finally, as pseudo observations, the recovered single-differenced ionospheric-free integer ambiguities are mapped back onto the undifferenced ambiguities and are strongly constrained within the precision orbit determination of Haiyang-2B. The details of ambiguity fixing process can be found in [11].

One must be aware that, according to (6), the bias errors may result in two consequences in the WL fixing. The first is these errors make the fixing decision fail directly because of the overly discrete distribution of the errors. The second is that the WL fixing is successful, but the WL estimate is biased. If the WL is shifted by ± 1 cycle, i.e., 86.2 cm, which is possible when the bias errors reach the meter level as for the $P1$ code observations, based on (8) the NL will be shifted by about ± 3.53 cycles. After correcting the FCBs, according to the theory of error, the float NL ambiguity should be located around the nearest integer cycle. However, the fractional part of the NL bias, 0.53 cycles, makes the NL ambiguity center around the half cycle. This also results in the failure of the ambiguity fixing. Generally speaking, both cases reduce the success rate of ambiguity fixing.

In the second case, since the NL is an integer, theoretically, we can use that fact to decide between two candidate WL ambiguities [27]. However, it is also easy to get some ambiguities fixed incorrectly. There are some unfixable NL ambiguities which may not be caused by the shifted WL. When adjusting the WL deviations by cycles, these NL ambiguities can meet the conditions of fixing decisions. Although the fixing success rate has been greatly improved by this means, we find that the incorrectly fixed ambiguities will seriously damage the precision of the orbit determination.

IV. RESULTS AND DISCUSSION

To analyze the code bias errors on the ambiguity resolution, we created different ambiguity-fixed POD solutions using the $C1$ and $P1$ codes with and without bias corrections and demonstrated their contribution to the ambiguity-fixed solutions.

A. Data Collection

In this article, we processed five months of early data from October 30, 2018 to March 27, 2019, and for further verification, we also collected the data from March 30, 2021 to June 1, 2021. This data was issued by the National Satellite Ocean Application Service, and the time span of the two sets of data was more than two years. The GPS precise orbits, integer-recovery clocks, and WL FCB products provided by CNES were used for the ambiguity resolution. The IGS final orbits and the 30-s clocks were used for the ambiguity-float solutions in this article.

TABLE II
DYNAMIC MODELS FOR THE HAIYANG-2B POD USING GPS

Item	Configuration
Earth gravity	EIGEN-06C, up to degree and order 120 for static
Solid Earth tide and pole	IERS 2010 [28]
Ocean tides	FES2004 30×30 [29]
Ocean pole tides	Desai [30]
Conventional inertial reference frame	Geocentric Celestial Reference Frame at J2000.0
Relativity	IERS 2010 [28]
N-body perturbation	JPL DE405
Earth orientation	IERS C-04
Atmosphere drag	DTM2013 [31], piece-wise drag coefficients were estimated every 180 min
Empirical accelerations	piece-wise periodical terms in the along- and cross-track directions were estimated every 180 min
Solar radiation pressure	Box-wing model, the scale parameter was estimated

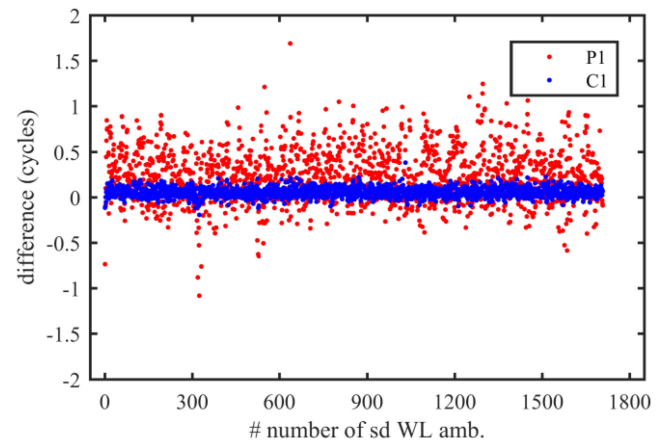


Fig. 14. Differences between the float WL ambiguities with and without the code bias corrections for the $C1$ and $P1$ solutions of the Dec. 9, 2018 data.

B. Ambiguity Fixing Rates in Orbit Determination

In the beginning, five months of early onboard GPS data was used to determine the ambiguity-float and ambiguity-fixed orbits of the Haiyang-2B satellite using an improved version of the positioning and navigation data analyst software. For the ambiguity-fixed solutions, the $C1$ and $P1$ code observations were used with and without the code bias corrections. It should be noted that the $C1$ code observations needed to be corrected using the external differential code bias (DCB) products. In order to further verify the stability of the static pattern, a grid correction of the code bias map was estimated using only the December 2018 data. Single-differenced ambiguities with a common observation time of fewer than 8 minutes were ignored, and the STD threshold value of the WL ambiguities for making the fixing decision was set to 0.24 cycles due to the occurrence of moderate 20 cm variations in the $C1$ and $P2$ code MP. We defined 30-hour observations as the orbit arc, and carefully considered the perturbation forces on the satellite. Tables II and III list the dynamic models and the observation models in detail, respectively.

TABLE III
 OBSERVATION MODELS FOR THE HAIYANG-2B POD USING GPS

Item	Configuration
Observation sampling	30 s
POD arc length	30 h
Observation choice	C1 or P1 code, P2 code, L1 carrier phase, and L2 carrier phase
DCB	Provided by CODE for the C1 code correction
Ionospheric delay	Ionospheric-free combination, high-order delay was neglected
Code bias	With and without the grid map correction
GPS precise orbit and clock	GRG orbit and integer-recovery 30s clock for the ambiguity-fixing solutions; IGS orbit and 30s clock for the ambiguity-float solutions
Wide-lane FCBs	Provided by CNES
GPS phase center	igs14.atx delivered by IGS
Phase windup	Correcting using published models
Elevation cutoff	0°
Initial state	Position and velocity at the initial epoch
Receiver clock	estimated as process noise, and one parameter per epoch
Ambiguities	One per pass
Wide-lane fixing decision	0.24 cycles
Narrow-lane fixing decision	0.12 cycles

Fig. 14 shows the differences in the single-differenced float WL ambiguities with and without code bias corrections. For the *P1* solutions, the differences are significant, and some are greater than 0.5 cycles. If they were fixed to the nearest integer, the WL ambiguities would be shifted, which would lead to failure in the NL ambiguity fixing. Compared to the *P1* solutions, the differences in the *C1* solutions are much smaller, and they are generally within 0.2 cycles. For a WL fixing decision of 0.24 cycles, the errors has very little effect on the ambiguity fixing of the *C1* solutions.

In Fig. 15, as expected, the WL ambiguity fixing rates of the *C1* solutions are not significantly affected by the code bias corrections. However, for the *P1* solutions, the WL fixing rates increased from $91.3\% \pm 1.6\%$ to $96.5\% \pm 1.0\%$, and the STD values decreased slightly. In addition, by comparing the *P1* and *C1* solutions without the code bias corrections, we find that the WL fixing rates are very close, but the NL fixing rate of the *P1* solution is much lower. This confirms that the code bias errors caused the biases in the WL ambiguities. As can be seen from Fig. 15, after applying the code bias corrections, although the fixing rate of the wide lane ambiguities only increased by 5.2%, the fixing rate of the narrow lane ambiguities increased from 71.8% to 87.4% with an improvement of 15.6%. The contribution of the code bias corrections was significant for *P1* solutions. As was previously mentioned, the grid code bias corrections were modeled using only the data for December 2018; and there was no significant decrease in the fixing rates in the other months. This also illustrates the stability of the static pattern. Therefore, the *P1* solutions only need a simple static correction model for ambiguity resolution, while the *C1* solutions rely on the external DCB products.

For further verification of the contribution of the code bias corrections, we processed the second set of data using the same strategy, except for the solution of the *C1* code using model corrections, as shown in Fig. 16. It can be seen that compared

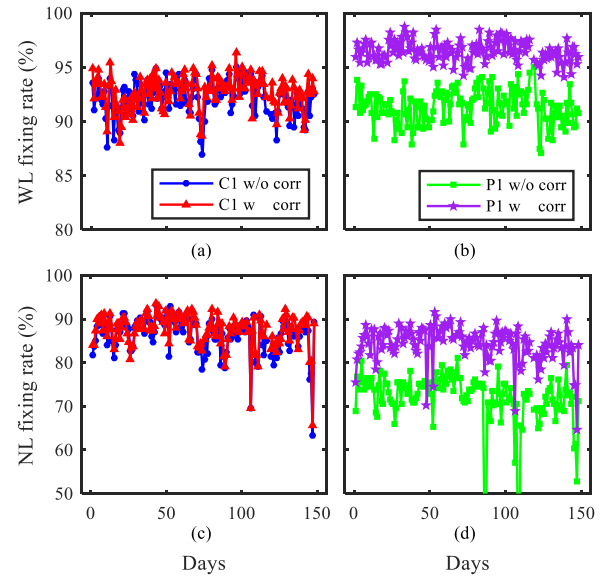


Fig. 15. WL and NL fixing rates of the *C1* and *P1* solutions with and without the code bias corrections based on five months of early data. (a) WL mean rates are $92.7\% \pm 1.5\%$ for the *C1* code with corrections, $92.2\% \pm 1.6\%$ for the *C1* code without corrections. (b) $96.5\% \pm 1.0\%$ for the *P1* code with corrections, and $91.3\% \pm 1.6\%$ for the *P1* code without corrections. (c) NL mean rates are $86.4\% \pm 4.2\%$ for the *C1* code with corrections, $87.4\% \pm 3.9\%$ for the *C1* code without corrections. (d) $87.4\% \pm 4.0\%$ for the *P1* code with corrections, and $71.8\% \pm 6.3\%$ for the *P1* code without corrections.

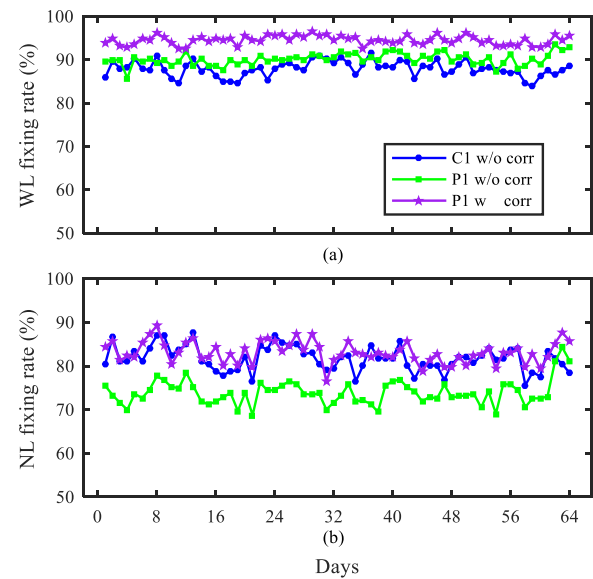


Fig. 16. WL and NL fixing rates of the *C1* and *P1* solutions based on data from April and May 2021. (a) WL mean rates are $87.9\% \pm 1.8\%$ for the *C1* code without corrections, $94.5\% \pm 1.0\%$ for the *P1* code with corrections, and $90.1\% \pm 1.4\%$ for the *P1* code without corrections. (b) NL mean rates are $81.7\% \pm 2.8\%$ for the *C1* code without corrections, $83.1\% \pm 2.5\%$ for the *P1* code with corrections, and $73.9\% \pm 2.8\%$ for the *P1* code without corrections.

with Fig. 15, the results were generally similar. Using the code bias corrections, the fixing rate of the narrow lane ambiguities still increased from 73.9% to 83.1%, with an improvement of 9.2%.

TABLE IV
MEAN AND STD OF THE INDIVIDUAL SLR STATION RESIDUALS FOR THE DIFFERENT SOLUTIONS

Station	#NP	Float amb. (cm)		C1 w/o corr. (cm)		C1 w corr. (cm)		P1 w/o corr. (cm)		P1 w corr. (cm)	
		mean	std	mean	std	mean	std	mean	std	mean	std
7090	2896	-0.59	1.45	-0.56	0.91	-0.58	0.92	-0.60	1.02	-0.57	0.88
7105	1040	0.08	1.39	0.06	1.13	0.07	1.15	0.08	1.18	0.07	1.18
7110	606	0.27	1.32	0.26	1.27	0.25	1.20	0.33	1.27	0.27	1.16
7237	1530	-1.38	1.98	-1.36	1.59	-1.35	1.62	-1.38	1.67	-1.35	1.61
7825	844	-0.95	1.08	-0.74	0.72	-0.75	0.71	-0.75	0.85	-0.70	0.79
7839	1115	1.10	1.74	0.71	1.20	0.72	1.19	0.85	1.53	0.71	1.25
7840	812	0.13	1.43	-0.09	1.02	-0.06	1.06	-0.06	1.31	-0.08	1.09
7841	361	-0.70	1.13	-0.67	0.86	-0.69	0.87	-0.58	0.97	-0.58	0.88
7941	871	-1.10	1.19	-0.98	0.98	-1.02	0.96	-1.09	1.06	-1.06	0.99
8834	501	-1.79	1.38	-1.93	1.15	-1.92	1.12	-1.94	1.37	-1.95	1.11
Total	10576	-0.42	1.63	-0.51	1.31	-0.52	1.31	-0.52	1.42	-0.52	1.32

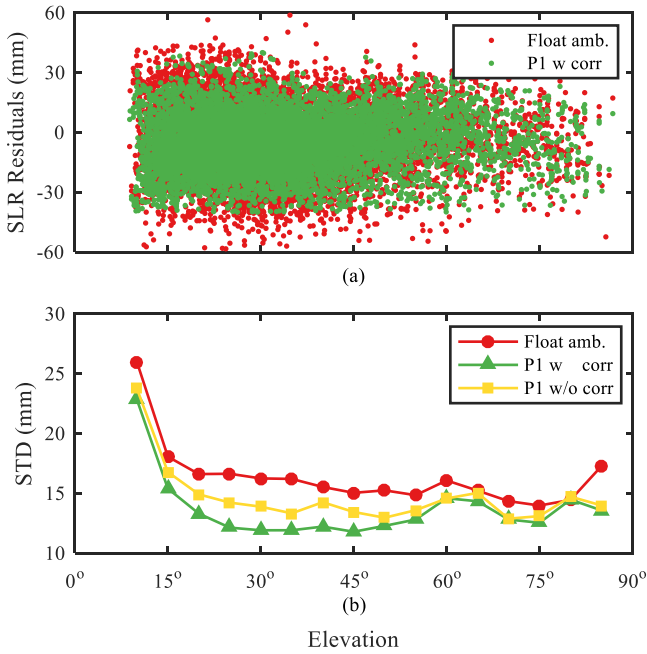


Fig. 17. SLR residuals and the 5° bin STD values of the ambiguity-float solutions and the $P1$ ambiguity-fixed solutions with (w) and without (w/o) code bias corrections versus the elevation for five months of early data.

C. SLR Validation

The SLR validation is an independent method of evaluating orbit accuracy. The SLR station coordinates are in reference to the SLRF2014 frame provided by the International Laser Ranging Service, which is consistent with the ITRF 2014 frame of the GPS orbit products.

Table IV gives the STDs of the SLR residuals of the individual stations used for the different POD solution validation, and Figs. 17 and 18, respectively, show the SLR residuals vary with elevation angles of the two sets of data. Compared to the ambiguity-float solutions, the improvement in ambiguity-fixed solutions is very significant. For 7090 station, which had the largest number of SLR observations, the STD of the SLR residuals decreased by 5.7 mm. The most prominent improvement (39.3%) occurred for the corrected $P1$ solutions. In addition, the average STD of all of the stations decreased by 19.6%. This

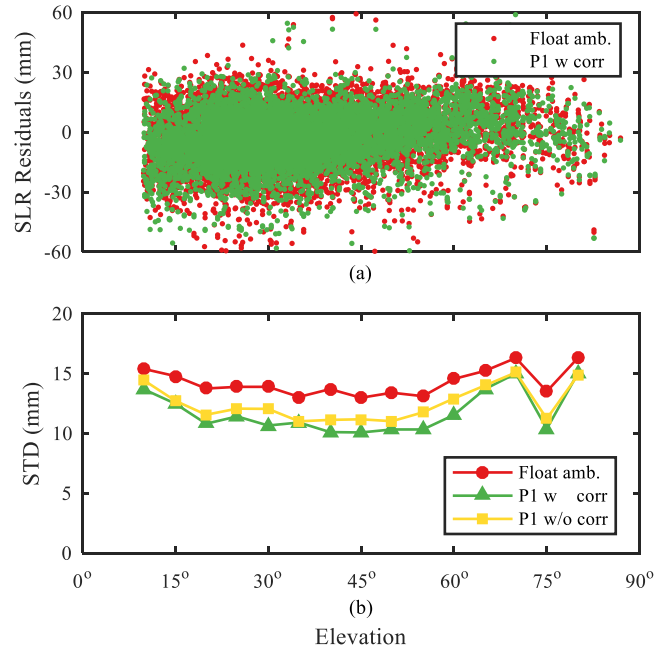


Fig. 18. SLR residuals and the 5° bin STD values of the ambiguity-float solutions and the $P1$ ambiguity-fixed solutions with (w) and without (w/o) code bias corrections versus the elevation for the data from April and May 2021.

indicates that the ambiguity resolution improves the accuracy of the orbit determination of Haiyang-2B.

As expected, there was no substantial improvement in the corrected $C1$ code solutions. However, for the $P1$ code, although the fixing rate of 71.8% in the solutions without corrections made the POD results better than the ambiguity-float solutions, the decrease of about 1–3 mm occurred due to the 15.6% increase in the fixing rate after applying the static corrections. This improvement was small but noticeable based on the STDs of the individual stations. The decrease was more significant for the mid-low elevations as can be seen from Figs. 17 and 18. Although the time span of the two sets of data is more than two years, it can be seen from the SLR residuals that the contribution of the code bias corrections was significant for $P1$ solutions, and the model correction method could still effectively improve the fixing success rate of the ambiguity of the HY2B satellite, thus improving the orbit determination accuracy.

V. CONCLUSION

In the POD processing, the code observations were critical to the ambiguity resolution. However, we found that the $P1$ code exhibited significant deviations compared to the $C1$ and $P2$ codes, especially for low elevation angles. These deviations did not cancel out during the single-differencing between the satellites. Since these errors are included in the computed MP errors, based on the MP combination equation, a static pattern was estimated using a grid map with a $5^\circ \times 5^\circ$ resolution. There was an obviously elliptical area in the center of the map, which varied within ± 10 cm, which is considered an acceptable range of fluctuations similar to that of the $C1$ and $P2$ code. However, outside of this area, the error increased rapidly and reached a maximum of 3 m in the crescent area between azimuth angles of 120° to 240° . In this article, we carefully analyzed the influence of the deviation errors of the $P1$ code on the ambiguity resolution.

We used two sets of onboard GPS data spanning more than two years to determine the orbit of the Haiyang-2B satellite. When only considering the noise level, the $P1$ code observations were more suitable for the ambiguity resolution, for which 90% of the STDs were less than 0.55 m. This is nearly 3.5 times smaller than that of the $C1$ code. However, the fixing rates of the NL ambiguities in the $C1$ solutions were almost 15% higher than those of the $P1$ solutions. When using the static code bias corrections for the $P1$ code, the fixing rates reached a level close to that of the $C1$ solutions, and the approximately 1–3 mm decrease in the STD of the SLR residuals was noticeable. By comparing the orbit determination solutions of the two sets of data, we verified the applicability of the grid model.

ACKNOWLEDGMENT

The authors are very grateful to IGS and CNES for providing the precise orbit and clock products. The authors would also like to thank LetPub (www.letpub.com) for its linguistic assistance during the preparation of this article.

REFERENCES

- [1] Z. Kang, P. Schwintzer, C. Reigber, and S. Zhu, "Precise orbit determination for TOPEX/Poseidon using GPS-SST data," *Adv. Space Res.*, vol. 16, no. 12, pp. 59–62, 1995.
- [2] T. Yunck *et al.*, "First assessment of GPS-based reduced dynamic orbit determination on TOPEX/Poseidon," *Geophys. Res. Lett.*, vol. 21, no. 7, pp. 541–544, Apr. 1994.
- [3] J. Ijssel, P. Visser, and P. Rodriguez, "Champ precise orbit determination using GPS data," *Adv. Space Res.*, vol. 31, no. 8, pp. 1889–1895, Apr. 2003.
- [4] O. Montenbruck and R. Kroes, "In-flight performance analysis of the CHAMP blackjack GPS receiver," *GPS Solutions*, vol. 7, no. 2, pp. 74–86, Jun. 2003.
- [5] Z. Kang, P. Nagel, and R. Pastor, "Precise orbit determination for GRACE," *Adv. Space Res.*, vol. 31, no. 8, pp. 1875–1881, Apr. 2003.
- [6] Z. Kang, B. Tapley, S. Bettadpur, J. Ries, P. Nagel, and R. Pastor, "Precise orbit determination for the GRACE mission using only GPS data," *J. Geodesy*, vol. 80, no. 6, pp. 322–331, Jul. 2006.
- [7] J. Ijssel, J. Encarnação, E. Doornbos, and P. Visser, "Precise science orbits for the swarm satellite constellation," *Adv. Space Res.*, vol. 56, no. 6, pp. 1042–1055, Sep. 2015.
- [8] J. Ijssel, B. Forte, and O. Montenbruck, "Impact of swarm GPS receiver updates on POD performance," *Earth, Planets Space*, vol. 68, no. 1, pp. 85–101, May, 2016.
- [9] Q. Zhao *et al.*, "Enhanced orbit determination for beidou satellites with FengYun-3C onboard GNSS data," *GPS Solutions*, vol. 21, no. 3, pp. 1179–1190, Feb. 2017.
- [10] J. Fernández, C. Fernández, P. Féménias, and H. Peter, "The copernicus sentinel-3 mission," in *Proc. Int. Laser Ranging Instrum. Workshop*, 2016, pp. 1–6, [Online]. Available: https://cddis.nasa.gov/lw20/docs/2016/papers/P32-Fernandez_paper.pdf
- [11] O. Montenbruck, S. Hacke, and A. Jäggi, "Precise orbit determination of the Sentinel-3A altimetry satellite using ambiguity-fixed GPS carrier phase observations," *J. Geodesy*, vol. 92, no. 7, pp. 711–726, Nov. 2018.
- [12] D. Arnold, O. Montenbruck, S. Hackel, and K. Sošnica, "Satellite laser ranging to low earth orbiters: Orbit and network validation," *J. Geodesy*, vol. 11, no. 93, pp. 2315–2334, Apr. 2018.
- [13] G. Blewitt, "Carrier phase ambiguity resolution for the global positioning system applied to geodetic baselines up to 2000 km," *J. Geophys. Res.*, vol. 94, no. B8, pp. 10187–10203, Aug. 1989.
- [14] M. Ge, G. Gendt, M. Rothacher, C. Shi, and J. Liu, "Resolution of GPS carrier phase ambiguities in precise point positioning (PPP) with daily observations," *J. Geodesy*, vol. 82, no. 7, pp. 389–399, Jul. 2008.
- [15] P. Collins, "Isolating and estimating undifferenced GPS integer ambiguities," in *Proc. Nat. Tech. Meeting Inst. Navig.*, Jan. 2008, pp. 720–732.
- [16] D. Laurichesse, F. Mercier, J. P. Berthias, P. Broca, and L. Cerri, "Integer ambiguity resolution on undifferenced GPS phase measurements and its application to PPP and satellite precise orbit determination," *Navig. J. Inst. Navig.*, vol. 56, no. 2, pp. 135–149, 2009.
- [17] J. Geng, X. Meng, A. Dodson, and F. Teferle, "Integer ambiguity resolution in precise point positioning: Method comparison," *J. Geodesy*, vol. 84, no. 9, pp. 569–581, Aug. 2010.
- [18] J. Geng *et al.*, "Improving the estimation of fractional-cycle biases for ambiguity resolution in precise point positioning," *J. Geodesy*, vol. 86, no. 8, pp. 579–589, Aug. 2012.
- [19] R. Hatch, "The synergism of GPS code and carrier measurements," in *Proc. 3rd Int. Symp. Satell. Doppler Positioning*, Feb. 1982, vol. 2, pp. 1213–1231, .
- [20] W. Melbourne, "The case for ranging in GPS-based geodetic systems," in *Proc. 1st Int. Symp. Precise Positioning Glob. Position. Syst.*, Apr. 1985, pp. 373–386.
- [21] G. Wübbena, "Software developments for geodetic positioning with GPS using TI-4100 code and carrier measurements," in *Proc. 1st Int. Symp. Precise Position. Glob. Positioning Syst.*, pp. 403–412, Apr. 1985.
- [22] F. Gao *et al.*, "Analysis of HY2A precise orbit determination using DORIS," *Adv. Space Res.*, vol. 55, no. 5, pp. 1394–1404, Mar. 2015.
- [23] C. Kee and B. Parkinson, "Calibration of multipath errors on GPS pseudorange measurements," in *Proc. 7th Int. Techn. Meeting Satell. Division, Inst. Navig.*, Sep. 1994, pp. 353–362.
- [24] K. Woo, "Optimum Semi-codeless carrier phase tracking of 12," *Navig. J. Inst. Navig.*, vol. 47, no. 2, pp. 82–99, 2000.
- [25] K. J., M. Li, Q. Zhao, W. Li, and X. Guo, "BeiDou geostationary satellite code bias modeling using Fengyun-3C onboard measurements," *Sensors*, vol. 17, no. 11, pp. 2460–2475, Oct. 2017.
- [26] S. Cheng, J. Wang, and W. Peng, "Statistical analysis and quality control for GPS fractional cycle bias and integer recovery clock estimation with raw and combined observation models," *Adv. Space Res.*, vol. 60, no. 12, pp. 2648–2659, Dec. 2017.
- [27] A. Leick, L. Rapoport, and D. Tatarnikov, *GPS Satellite Surveying*, 4th ed.. New York, NY, USA: Wiley, 2015, pp. 389–391.
- [28] G. Petit and B. Luzum, "IERS conventions 2010," IERS Convention Center, Int. Earth Rotation Ref. Syst. Service, IERS Technical Note No. 36, Frankfurt, Germany, 2010.
- [29] F. Lyard, F. Lefevre, T. Letellier, and O. Francis, "Modelling the global ocean tides: Modern insights from FES2004," *Ocean Dyn.*, vol. 56, no. 5, pp. 394–415, Sep. 2006.
- [30] S. Desai, "Observing the pole tide with satellite altimetry," *J. Geophys. Res.*, vol. 107, no. C11, pp. 3186–3192, Nov. 2002.
- [31] S. Bruinsma, "The DTM-2013 thermosphere model," *J. Space Weather Space Clim.*, vol. 5, no. A1, pp. 1–8, Feb. 2015.



Hailong Peng received the Ph.D. degree in ocean information exploration and data processing from the College of Information Science and Engineering, Ocean University of China, Qingdao, China, in 2015.

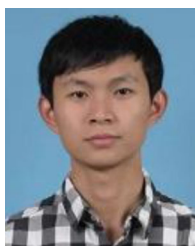
He is currently the Director Designer in charge of the Chinese HY-2 satellite precision orbit determination subsystem with the National Satellite Ocean Application Service, Beijing, China. He played an important role in model developing and the Operational data processing software designing for the HY-2 satellite precision orbit determination subsystem.

His main research interests include precision orbit determination, ocean microwave calibration and validation.



Rongxin Fang received the B.S. degree in geomatics engineering and M.S. degree in geodesy and surveying engineering from the Wuhan University, Wuhan, China, in 2010.

From 2011 to 2013, he finished two-year Postdoctoral Research with GNSS Research Center in Wuhan University, where he is currently an Associate Professor with GNSS Research Center. His main research interests include multi-GNSS precise positioning and its applications.



Kecai Jiang received the B.S. degree in geomatics engineering from Central South University, Changsha, China, in 2013, and the Ph.D. degree in geodesy and surveying engineering from Wuhan University, Wuhan, China, in 2020.

He is currently a Postdoctoral Researcher with Wuhan University. His current research mainly focuses on LEO and side-lobe signal HEO orbit determination using GNSS.



Mingsen Lin (Member, IEEE) received the Ph.D. degree in computing mathematics from the Computing Center, Chinese Academy of Sciences, Beijing, China, in 1992.

He is currently the Chief Designer of ground application system for HY-1 and HY-2 satellites, where he organized the argument of Chinese Ocean Satellite outline, and managed the construction of ground application system for Chinese Ocean Satellite with the National Satellite Ocean Application Service, Beijing.

He is also the Founder of satellite ocean remote sensing in China. He plays an important role in the development of Chinese Ocean Satellite and Manned Space Flight. His research interests include remote sensing of the ocean and computation fluid dynamics.



Min Li received the B.S. and Ph.D. degrees in geodesy and surveying engineering from Wuhan University, Wuhan, China, in 2005 and 2011, respectively.

He was a Research Fellow with the Hong Kong Polytechnic University, and is currently a Professor of GNSS Research Center, Wuhan University. His research interests include GNSS satellite orbit determination and precise point positioning as well as multi-GNSS processing using GPS, GLONASS, BeiDou, and Galileo.



Qile Zhao received the Ph.D. degree in geodesy and surveying engineering from Wuhan University, Wuhan, China, in 2004 and the M.S. degree in geodesy and surveying engineering from the Institute of Geology, China Earthquake Administration, Wuhan, in 1998.

During 2006–2007, he was a Postdoctoral Fellow, he did his postdoctoral program in DEOS, Delft University of Technology, Delft, the Netherlands. He is currently a Professor with the GNSS Research Center, Wuhan University. His current research interests are

precise orbit determination of GNSS and low earth orbit satellites, and high-precision positioning using GPS, Galileo and BeiDou system.



Youcun Wang received the M.S. degree in geomatics engineering from the Shandong University of Science and Technology, Qingdao, China, in 2019. He is currently working toward the doctoral degree in geodesy and surveying engineering at Wuhan University, Wuhan, China.

His main research interests include the precision orbit determination of LEO and dynamics model refinement.



Xiaomei Wang received the B.S. degree in automation from Northwestern Polytechnical University, Xi'an, China, in 1991.

She is currently a Senior Engineer and a Designer in charge of the Chinese HY-2 satellite precision orbit determination subsystem with the National Satellite Ocean Application Service, Beijing, China. Her main research interests include precision orbit determination and ocean color algorithms.